Hydrol. Earth Syst. Sci. Discuss., 11, 5077–5114, 2014
www.hydrol-earth-syst-sci-discuss.net/11/5077/2014/
doi:10.5194/hessd-11-5077-2014

Hydrology and Earth System Sciences
Open Access
Discussions

Climate change and non-stationary flood risk for the Upper Truckee River Basin

L. E. Condon[1,2], **S. Gangopadhyay**[1], **and T. Pruitt**[1]

[1]Bureau of Reclamation, Technical Service Center, Denver, Colorado, USA
[2]Hydrologic Science and Engineering Program and Department of Geology and Geological Engineering, Colorado School of Mines, Golden, Colorado, USA

Received: 23 April 2014 – Accepted: 25 April 2014 – Published: 16 May 2014

Correspondence to: L. E. Condon (lcondon@mymail.mines.edu)

Published by Copernicus Publications on behalf of the European Geosciences Union.

Abstract

Future flood frequency for the Upper Truckee River Basin (UTRB) is assessed using non-stationary extreme value models and design life risk methodology. Historical floods are simulated at two UTRB gauge locations, Farad and Reno using the Variable Infiltration Capacity (VIC) model and non-stationary Generalized Extreme Value (GEV) models. The non-stationary GEV models are fit to the cool season (November–April) monthly maximum flows using historical monthly precipitation totals and average temperature. Future cool season flood distributions are subsequently calculated using downscaled projections of precipitation and temperature from the Coupled Model Intercomparison Project Phase-5 (CMIP-5) archive. The resulting exceedance probabilities are combined into a single risk metric using recent developments in design life risk methodologies. This paper provides the first end-to-end analysis using non-stationary GEV methods coupled with contemporary downscaled climate projections to demonstrate how the risk profile of existing infrastructure evolves with time over its design life. Results show that flood risk increases significantly over the analysis period (from 1950 through 2099). This highlights the potential to underestimate flood risk using traditional methodologies that do not account for time varying risk. Although model parameters, for the non-stationary method are sensitive to small changes in input parameters, analysis shows that the changes in risk over time are robust. Overall, flood risk at both locations (Farad and Reno) is projected to increase 10–20 % between the historical period 1950–1999 and the future period 2000–2050 and 30–50 % between the same historical period and 2050–2099.

1 Introduction

"Stationarity is Dead ..." (Milly et al., 2008), yet the standard practice for flood frequency analysis is predicated on this very assumption. This discrepancy has not gone unnoticed within the scientific community and there is a growing body of research

HESSD
11, 5077–5114, 2014

investigating, (1) trends in observed floods (e.g., Franks, 2002; Vogel et al., 2011), (2) ways to incorporate non-stationarity into frequency distributions (e.g., Katz and Neveau, 2002; Raff et al., 2009) and (3) methodologies to interpret risk within a non-stationary framework (e.g., Rootzen and Katz, 2013; Salas and Obeysekara, 2014). Both the frequency and intensity of extreme events are particularly susceptible to change because small shifts in the center of a distribution can potentially have much larger impacts on the tails (Meehl et al., 2000). Regardless of climate change, naturally occurring long-term climate oscillations, such as ENSO, have been linked to low frequency variability in flood frequency (e.g., Cayan et al., 1999; Jain and Lall, 2001). Anthropogenic climate change has the potential to amplify this variability by introducing additional non-stationarity to interconnected climate and hydrologic systems.

Already trends in many hydrologic variables have been observed across the western US. For example, clear increases in temperature have been measured across the West (e.g., Cayan et al., 2001; Dettinger and Cayan, 1995). Precipitation trends are more variable. Regonda et al. (2005) found increased total winter precipitation (rain and snow) from 1950 to 1999 in many sites across the western US, although springtime snow water equivalent (SWE) was shown to decline over the same period. Similarly, Mote et al. (2005) analyzed snowpack trends in western North America, and reported widespread declines in springtime SWE over the period 1925–2000, especially since the middle of the 20th century. They attribute this decline predominantly to climatic factors such as El Niño–Southern Oscillation (ENSO), Pacific Decadal Oscillation (PDO), and positive trends in regional temperature. Easterling et al. (2000) summarized previous studies on precipitation trends. They note that trends vary from region to region, but in general, increases in precipitation have occurred disproportionately in the extremes. Several subsequent studies have observed increasing trends in extreme precipitation events, although the changes are relatively small (Gutowski et al., 2008; Kunkel, 2003; Madsen and Figdor, 2007).

Similarly, research has demonstrated increasing trends in flood frequency in some regions. Walter and Vogel (2010) and Vogel et al. (2011) observed increasing flood

HESSD
11, 5077–5114, 2014

magnitudes across the US using stream gauge records, and Franks (2002) showed statistically significant increases in flood frequency since the 1940s. Still, flooding trends have been historically difficult to quantify and there has been some debate on the significance of flood frequency trends. For example, Douglas et al. (2000) found that if one takes into account spatial correlation, many previous findings of flood trends are not statistically significant. Even when significant trends are found, the complexity of flooding mechanisms that depend on many variables and can vary regionally and seasonally make it difficult to attribute trends to specific causes. Illustrating the importance of seasonality, Small et al. (2006) showed that if a high precipitation event occurs in the fall, as opposed to the spring, it will contribute to baseflow rather than inducing flooding. Also, urbanization can drastically increase the impervious area of a basin, thus amplifying floods by decreasing infiltration and speeding runoff. The largest flood magnitude increases observed by both Walter and Vogel (2010) and Vogel et al. (2011) were in basins with urban development. The influence of development trends on flood behavior can be difficult to separate from other variables. For example, Villarini et al. (2009) could not conclusively tie reduced stationarity (i.e., changes in mean and/or variance) in peak discharge records to climate change because of variability in the other factors that influence runoff.

Setting aside the impacts of development and management practices, future extremes can be influenced by a number of interrelated variables such as changes in temperature, precipitation efficiency, and vertical wind velocity (Mullet et al., 2011; O'Gorman and Schneider, 2009). Analyzing global circulation model (GCM) outputs Pierce et al. (2012) found total changes in precipitation to be small relative to the existing variability but noted larger seasonal changes in storm intensity and frequency. Despite uncertainty, many studies agree that warming will increase the potential for intense rainfall (Allan, 2011; Gutowski et al., 2008; Pall et al., 2011; Sun et al., 2007). Furthermore, Min et al. (2011) found that some GCM simulations may underestimate extreme precipitation events in the Northern Hemisphere. Indicating that projections of extreme precipitation based on GCM outputs may be conservative.

HESSD
11, 5077–5114, 2014

Studies have also predicted increases in flood frequency and magnitude with a warmer climate, especially in snowmelt dominated basins (e.g., Das et al., 2011). As with historical flooding trends, translating forecasted climate variables to flood frequency is a complex process and several methodologies have been used. Downscaled GCM climate forcings can be used to drive hydrologic models and simulate future floods directly (e.g., Das et al., 2011; Vogel et al., 2011; Raff et al., 2009). With this approach traditional stationary flood frequency distributions can be fit to the simulated floods to calculate return periods of interest (e.g., Raff et al., 2009; Vogel et al., 2011). This allows for return periods and flood magnitudes that change over time, as with the flood magnification and recurrence reduction factors calculated by Walter and Vogel (2010) and Vogel et al. (2011). However, these approaches still assume flood mechanisms are stationary over the time period that the distribution is fit to.

This limitation can be overcome using non-stationary generalized extreme value (GEV) distributions where the model parameters like mean (i.e., location) and spread (i.e., scale) are allowed to vary as a function of time (e.g., Gilroy and McCuen, 2012) or with relevant covariates (e.g., Griffis and Stedinger, 2007; Katz et al., 2002; Towler et al., 2010). This approach has been gaining popularity for flood frequency estimation. Using this technique, it is not necessary to simulate future floods directly by forcing a hydrologic model with projected hydroclimate fields (e.g., precipitation and temperature). The parameters of the GEV model, like mean and spread change with time (i.e., non-stationary) based on a linear combination of covariates like precipitation and temperature. Historical relationships between extreme events and hydroclimate fields are used to identify the weighting of covariates. These weights are then used to estimate parameters for future time periods using precipitation and temperature outputs from hydroclimate projections. For example, Gilroy and McCuen (2012) used non-stationary GEV models of flood frequency that incorporated a linear trend in the location parameter. Similarly, Griffis and Stedinger (2007) and Towler et al. (2010) used climate variables as covariates for the distribution parameters.

HESSD
11, 5077–5114, 2014

While non-stationary flood forecasting methods provide flexibility to analyze flood variability, they are also incongruent with many of the traditional risk metrics used in water resources planning. Historically, most flood infrastructure has been designed to withstand flooding of specified return period (e.g., the 100 year flood). However, these calculations rely on a flood distribution which is assumed to remain stationary with time, and hence the return period design metric is also assumed to be stationary. When non-stationary methods are used, the underlying flood distributions, and associated return periods, vary with time. Thus, under a non-stationary climate, the notion of static return period flood event (e.g., 100 year flood, 200 year flood, etc.) is no longer a valid concept.

To address this issue, Rootzén and Katz (2013) introduced the concept of design life level to calculate the risk of a given flood magnitude occurring over a specified time period. Salas and Obeysekera (2014) further demonstrated the relevance of this technique to hydrologic community using flood frequency examples. However, this methodology still has yet to receive widespread attention within the hydrologic community. Here, we present a non-stationary flood frequency assessment for the Upper Truckee River Basin (UTRB) using contemporary downscaled climate projections and the non-stationary design life level technique introduced by Rootzén and Katz (2013) to quantify flood risk. This paper provides an end-to-end demonstration of non-stationary GEV analysis coupled with contemporary downscaled climate projections (specifically, downscaled climate projections from the Coupled Model Intercomparison Project Phase-5 (CMIP-5)), to quantify how the risk profile of existing infrastructure, designed on the basis of a specified flood event, evolves with time over its design life.

The paper is organized as follows. Section 2 provides background on the study area along with data sets used. The methodologies of using non-stationary spatial GEV analysis in conjunction with climate projections and time evolving risk assessment are described in Sect. 3. Results and discussions of findings are given in Sect. 4. Summary and conclusions from the analysis are presented in Sect. 5.

HESSD
11, 5077–5114, 2014

2 Background

This section provides background on the study area (Sect. 2.1), streamflow simulation and validation (Sect. 2.2) and climate data (Sect. 2.3).

2.1 Upper Truckee River Basin

The Truckee River originates in northern Sierra Nevada Mountains in California (above Lake Tahoe) and flows northeast to Nevada where it ends in the Pyramid Lake (Fig. 1). The total basin area is roughly 3060 square miles however the area upstream of Reno (1067 square miles) provides the majority of the basin's precipitation through snowpack. The focus of this analysis is on the Farad and Reno gauge locations shown in Fig. 1, henceforth referred to as Farad and Reno. The Farad gauge is located roughly one mile downstream of the Farad hydropower plant and provides a cumulative measure of all of the upper basin tributaries (Stokes, 2002). The Reno gauge is located downstream of Farad in the heart of Reno Nevada (the fourth largest city in the state of Nevada with a population of roughly 225 000 according to the 2010 census) and is a good reference point for analyzing urban flooding.

Flooding in the upper Truckee generally takes one of three forms. Some of the most severe floods have resulted from heavy rain events covering most of the basin and lasting one to six days. These storms generally occur from November to April and may be linked to Atmospheric Rivers (Ralph and Dettinger, 2012). Snowmelt floods are also common from April to July. Although, snowmelt floods transmit large volumes of water for longer durations, they generally do not cause damage because they are well predicted and can be regulated with upstream reservoirs. Finally, in late summer (July–August) local cloudbursts can generate high intensity precipitation over small areas. These storms can cause local damage to tributaries but generally do not have a large impact on the main stem of the Truckee.

In the twentieth century, nine major floods have been recorded on the Truckee River, all of which occurred from November to April (USACE, 2013). The flood of record

HESSD
11, 5077–5114, 2014

occurred in January of 1997 and was caused by warm rain falling on a large snowpack (~ 180 % of normal) and melting nearly all of the snowpack below 7000 feet (USACE, 2013). The floods of 1950, 1955 and 1963 were some of the most damaging due to the development of Reno along the river during this time period (USACE, 2013). Subsequent flood damages have been, at least partially, mitigated by the implementation of flood infrastructure starting in the 1960s.

2.2 Streamflow data

Streamflow has been measured at both the Farad and Reno USGS gauges. However, gauge flows are not readily applicable to flood frequency analysis due to the presence and development of water supply and flood control structures upstream. For example, upstream of Reno there are four dams with flood control capabilities (i.e., Martis Creek Dam, Prosser Creek Dam, Stampede Dam and Boca Dam) in addition to Tahoe, Donner and Independence Lakes which provide incidental flood regulation. Unregulated flow estimates were developed by the US Army Corps of Engineers (USACE) but are only available for historical flood periods (USACE, 2013). Therefore, we simulate unregulated flows from 1950 to 1999 using the Variable Infiltration Capacity (VIC) model and validate results using the available unregulated flow estimates.

A brief summary of the VIC model is provided here, and for additional technical specifications the reader is referred to Liang et al. (1994, 1996) and Nijssen et al. (1997). VIC is a gridded hydrologic model designed to simulate macro scale (spatial resolution greater than 1 mile) water balances using parameterized sub-grid infiltration and vegetation processes. In the VIC model, surface water infiltrates to the subsurface based on conductivity, and soil moisture is distributed vertically through three model layers extending up to about 2 m below the land surface. At the surface, potential evapotranspiration (PET) is simulated using the Penman Monteith PET model (Maidment et al., 1993). Surface flows are determined in a two-step process. First, the water balance for each grid cell is calculated independently to determine surface runoff and baseflow, and subsequently runoff from each cell is routed to river channels and outlets using

HESSD
11, 5077–5114, 2014

a predefined routing network. Here we drive VIC with daily weather forcings including precipitation, maximum and minimum temperature and wind speed. Additional weather variables such as short and long wave radiation, relative humidity and vapor pressure are calculated within the model. The VIC model is well documented and has already been used in a number of hydrologic and climate change studies (e.g., Christensen and Lettenmaier, 2007; Christensen et al., 2004; Gangopadhyay et al., 2011; Maurer et al., 2007; Payne et al., 2004; Reclamation, 2011; Van Rheenen et al., 2004). Recently VIC has also been applied for real time flood estimation (Wu et al., 2014). We provide additional model verification for flood simulation in the UTRB in subsequent sections.

2.3 Climate data

As noted in the previous section, the VIC model requires daily weather inputs to drive water balance simulations. We use the national 1/8° (roughly 7 miles) gridded dataset from Maurer et al. (2002) for historical (i.e., 1950–1999) climate observations. Additionally, monthly total precipitation and average temperature were aggregated for the upstream area of each gauge for every month of the flood season (i.e., November through April). These values are used as covariates for fitting non-stationary GEV models as discussed in Sect. 3.

Additional gridded precipitation and temperature values from 1950 to 2099 were generated from Global Circulation Model (GCM) outputs. We analyzed 234 projections generated by 37 different climate models from the CMIP-5 (Coupled Model Intercomparison Project Phase 5) archive (Taylor et al., 2012). The GCM simulations span four Representative Concentration Pathways (RCPs) for greenhouse gas emissions. Each GCM simulation includes monthly gridded precipitation and temperature from 1950 to 2099 at a coarse grid resolution ranging between ∼ 40–160 miles.

The Bureau of Reclamation in collaboration with other federal and non-federal partners has developed a monthly archive of downscaled CMIP-5 projections at the finer 1/8° resolution using the two-step BCSD (Bias Correction and Spatial Disaggregation)

HESSD
11, 5077–5114, 2014

algorithm described in Wood et al. (2004). The downscaled weather variables include monthly total precipitation, monthly maximum and minimum temperatures and monthly average temperature. Before applying the BCSD algorithm all the 234 GCM climate simulations were first gridded from their respective native GCM scale to a common grid of 1° latitude by 1° longitude. Similarly, the observed 1/8° gridded dataset (Maurer et al., 2002) was aggregated to the coarser 1° latitude by 1° longitude grid. Next, for a given climate variable, GCM, and location (1° latitude by 1° longitude grid cell), the bias correction (BC) step uses quantile mapping between monthly CDFs (Cumulative Distribution Functions) of historical GCM simulated and historical observed values to identify biases over a common climatological period – in this case, 1950–1999. The projected future (i.e. 2000–2099) weather variables from the same GCM at the same location are then bias corrected using the identified bias. The result of bias-correction is an adjusted GCM dataset (20th century and 21st century, linked together) that is statistically consistent with the observed data during the bias-correction overlap period (i.e., 1950–1999 in this application). Note that the BC step happens at the coarse 1° latitude by 1° longitude grid. Next, adjustment factors that are multiplicative (ratio of bias-corrected GCM to observed) for precipitation and an offset (bias-corrected GCM minus observed) for temperature are calculated for each of the 1° latitude by 1° longitude grid cell (Reclamation, 2013). These adjustments are then spatially disaggregated (SD) to a 1/8° latitude by 1/8° longitude grid. Finally, the adjustments are applied (multiplicative for precipitation; additive for temperature) to the finer resolution, 1/8° gridded observed precipitation and temperature fields (Maurer et al., 2002) to derive the 1/8° gridded BCSD climate projections.

3 Methodology

This section describes the methodology used for flood frequency analysis in the UTRB. Discussion is divided into two sections. First, we describe the process of extreme value

HESSD
11, 5077–5114, 2014

modeling using non-stationary GEV distributions (Sect. 3.1). Second, the methodology for design life level risk assessment is detailed (Sect. 3.2).

3.1 Extreme value modeling

Extreme values analysis (EVA) deals with the examination of the tail (i.e., extreme) values of a distribution (as opposed to standard approaches which are generally more concerned with the average system behaviour). EVA methods are standard practice for flood frequency analysis because they are designed to capture the behaviour of low frequency high impact events. Furthermore, in climate change studies Katz (2010) points out that traditional approaches are not sufficient and extreme value statistics are needed. For this analysis, we use the Generalized Extreme Value (GEV), which is commonly applied to flood frequency analysis to model block maxima from streamflow time series (e.g., Katz et al., 2002; Towler et al., 2010). The cumulative distribution function (CDF) for the GEV is as follows:

$$F(z;\theta) = \exp\left\{-\left[1+\xi\left(\frac{z-\mu}{\sigma}\right)^{-\frac{1}{\xi}}\right]\right\} \quad (1)$$

where z is the streamflow maxima value of interest and θ is the parameter set (μ, σ, ξ) used to specify the distribution such that the center is given by the location (μ), the spread by the scale (σ) and the behavior of the upper tail by the shape (ξ). Based on the shape parameter, the GEV can take one of three forms: Gumbel, or light tailed, when ξ is zero; Fréchet, or heavy tailed, if ξ is positive; and Weibull, or bounded, when ξ is negative. Following the methodology of Towler et al. (2010), GEV parameters (μ, σ, ξ) are fitted using the Maximum Likelihood Estimation (MLE) technique.

In traditional stationary flood frequency analysis, it is assumed that observations are independent and identically distributed (IID), and therefore model parameters (μ, σ, ξ) are derived from the observed flood record and are assumed to remain constant across the period of record and into the future. Here, we introduce non-stationarity

HESSD
11, 5077–5114, 2014

into the distribution by allowing location and scale parameters to change with relevant covariates. Such that:

$$\mu(t) = \beta_{0,\mu} + \beta_{1,\mu}x_1 + \ldots + \beta_{n,\mu}x_n \quad (2)$$

$$\sigma(t) = \beta_{0,\sigma} + \beta_{1,\sigma}x_1 + \ldots + \beta_{n,\sigma}x_n \quad (3)$$

where the β variables represent the coefficients, and the x variables are the covariates.

To determine the optimal set of covariates for a non-stationary model, additional statistical methods must be employed. The Akaike Information Criterion (AIC; Akaike, 1974), given in Eq. (4), weighs the goodness of fit for a model with the level of complexity.

$$\mathrm{AIC} = -2(\mathrm{llh}) + 2K \quad (4)$$

Here llh is the negative log likelihood estimated for a model fitted with K parameters. In this formulation, higher ranked models have lower AIC scores. For this analysis the best model is selected using pairwise comparisons of AIC scores and significance tests to ensure statistically significant (threshold of 0.05) differences between scores.

Following the methodology described above, GEV distributions are fit to time series of maximum monthly historical (1950–1999) one day simulated stream flows (detailed in Sect. 2) for the cool season. The dataset includes maximum daily streamflows for each month in the cool season defined by the block of months November through April, as opposed to the more traditional single value per year. This technique was also used by Towler et al. (2010) who noted that expanding the dataset helps avoid the problems associated with using maximum likelihood estimate on small datasets. Floods during the cool season generally last between one and four days. Here we focus on the one day flood peak, as opposed to multi-day flood volumes, because this is a representative metric for flood damage. Additionally, using the one day flood maximum focuses the analysis on flood magnitude rather than duration.

Two covariates were considered, monthly total precipitation (P) and mean temperature (T) averaged over the upstream area for each gauge. As discussed in Sect. 2,

HESSD
11, 5077–5114, 2014

precipitation is a relevant covariate because many of the floods in this season are rain on snow events or extreme rainfall events. Similarly, temperature drives snowmelt and is an important contributor to UTRB flood events (e.g., January 1997 event). Both stationary and non-stationary GEV models were evaluated using the extRemes package (Gilleland and Katz, 2011) in the "R" statistical computing environment.

3.2 Time varying risk assessment

Traditional flood planning relies on the concept of return periods, which are usually calculated as the inverse of annual exceedance probability for a given flood magnitude, assuming a stationary distribution. For example, the log-Pearson Type III (LP3) distribution described by the Interagency Advisory Committee on Water Data Bulletin 17B (IACWD, 1982). However, when non-stationary models are used, the distribution parameters, and hence the exceedance probabilities vary with time. Table 1 compares various flood probability calculations between stationary and non-stationary approaches (Salas and Obeysekera, 2014). As shown here, when the flood distribution is stationary, the return period for a given flood magnitude is constant and relies only on the exceedance probability (4a). However, if distribution parameters are non-stationary then the return period will vary based on the period of interest (4b). This concept is easily extended to flood risk. In traditional analyses, the risk of a flood occurring in a given period depends only on the length of the period (5a), while in a non-stationary analysis risk depends on both the length of time considered and the time period itself (5b). This is the concept of design life level proposed by Rootzén and Katz (2013). Here, we adopt the design life level risk framework given in (5b) and calculate the risk of flood for a range of future periods and design life lengths.

HESSD
11, 5077–5114, 2014

4 Results and discussion

Results are grouped into three sections. First, we present the development of the non-stationary GEV models (Sect. 4.1). Next the models are verified by comparing simulated results to observations (Sect. 4.2). Finally, we present future projections of flood frequency analysis (Sect. 4.3).

4.1 Extreme value model development

A suite of models were fit to the logarithms of block (cool season, November–April) maxima flows (simulated by VIC) with different non-stationary parameter combinations The model structures tested include stationary, non-stationary location, non-stationary scale and non-stationary location and scale. For all model structures, model fit was tested using one or both covariates (i.e., precipitation and temperature) from the historical, 1950–1999, weather data. Models were also tested using the block maxima flows directly; however, performance was improved considerably with the logarithmic transformation. Validation of the VIC simulated flows as well as the GEV models are presented in the following section.

Table 2 summarizes negative log-likelihood (NLLH) scores for each model configuration and the p values of pairwise comparisons of AIC scores (note that the bottom row provides the model number that was used for the pairwise comparisons). As shown here, the models with non-stationary location and scale relying on both precipitation and temperature as covariates have the best (i.e., lowest) NLLH scores for both stations, and are a statistically significant improvement over the other models listed in Table 2. Figure 2 plots, stationary and non-stationary location and scale models with histograms of observed flow for both gauges. Qualitatively, the stationary model fits well with the center of the distribution but overestimates the tails. The non-stationary models overestimate the median values but are a closer fit to the extreme values.

The coefficients for Eqs. (2) and (3) for the selected models are provided in Table 3. Using the coefficients determined from the historical, 1950–1999, weather data, the

HESSD
11, 5077–5114, 2014

location and scale and shape are calculated for every GCM climate simulation (i.e., 234) and flood season month (i.e., November to April 1950 to 2099) based on the downscaled precipitation and temperature values detailed in Sect. 2. Thus, for every future month there is a separate GEV curve for each of the 234 climate simulations.

4.2 Hydrologic and GEV model validation

Because we utilize modeled VIC flows for flood analysis, there are two considerations for model validation. First, we compare VIC simulated one day flood events to the observed ungauged flow estimates. Second, we compare the GEV modeled floods to the VIC simulated flows and the observed flow estimates.

Although, ungauged flows are not available for the entire period of record, one-day maximum ungauged flow estimates are available at Reno for six historical floods (USACE, 2013). Figure 3 plots the observed flow (blue triangle) with the one-day VIC flow that was simulated using historical observed forcings from Maurer et al. (2002) (red triangle), and a boxplot of the non-stationary GEV distribution for the same month generated using the same monthly historical precipitation and temperature (i.e., Maurer et al., 2002). Comparing first the one day maximum VIC simulated flow with the observed flow there is generally good agreement between the two, although there appears to be a slight positive bias in the VIC simulations (i.e., VIC simulated flows are greater than observed flood flows). Still, the simulated flood values generally fall within the interquartile range of the GEV distribution, except in the case of the 2 February 1963 flood and the 2 January 1997 flood.

In these instances the VIC simulation matches very closely with the observed flow, however, the GEV model underestimates the events. This discrepancy is caused by the flood timing. In both cases the flood occurs at the very beginning of the month. In the GEV framework the precipitation and temperature are used as covariates for the flow of the same month. However, for these storms flooding is linked to precipitation and temperature in the month of flooding and the preceding month. Therefore, the GEV model simulates the flood in the preceding month and/or underestimates the flood

HESSD
11, 5077–5114, 2014

magnitude if the precipitation is split between two months. While this is a limitation for matching individual historical events, primarily timing, it is not a major concern in future projections. This is because, for the purposes of risk calculations, it really does not matter in which month the GEV model simulates the flood event as long as it realistically captures flood magnitude behavior.

Comparing the GEV model distribution to the other observed floods, the distribution encompasses the observed flood magnitude (within the 5th and 95th percentile) for all except for two of the floods (1955 and 1963). For 1963, the VIC simulated and observed floods are in close agreement and the discrepancy with the GEV model is explained by the flood timing described above. The 1955 flood resulted from 15 inches of melted snow combined with 13 inches of rainfall over a three day period. In the historical forcings used to drive the VIC model December 1955, has 29.6 inches of precipitation, which is the highest December precipitation value in the historical period. In this instance, the GEV model is in good agreement with the VIC simulated flow but the high monthly precipitation results in an overestimation of the flood magnitude. Again, this is a limitation of using monthly forcings because the total December precipitation is used as a covariate and not a storm specific value, though in many cases the storm specific values constitute the bulk of the monthly precipitation totals.

In general, we note good agreement between simulated and observed flood magnitudes even though Fig. 3 illustrates some of the complications in matching individual events. Figure 4 is a time series plot of VIC historical simulated flow along with the median and 5th to 95th percentile flow of the GEV model. As would be expected from the model fit demonstrated in Figs. 2 and 3, Fig. 4 shows that the VIC simulated flows are generally close to the median GEV modeled flow and nearly always fall within the 5th to 95th percentile range. Although there are differences in the simulation of individual events discussed above, the median simulated flood magnitudes are only greater than the maximum observed flood in two instances. This demonstrates that the model behavior is a reasonable match to the natural system.

HESSD
11, 5077–5114, 2014

4.3 Future flood risk

Future flood risk is calculated using Eq. (5b) from Table 1. For the first part of this analysis we define "flood" as one-day flow exceeding 37 600 cfs. This is the maximum historical ungauged flow at Reno from the 2 January 1997 event and is considered to be the design flood for flood protection infrastructure design. For each simulation month (1950–2099 November–April) exceedance probabilities are calculated for every GCM climate simulation (234 in total) using the selected non-stationary GEV model coefficients and parameters from Table 3 and the GCM simulated monthly precipitation and temperature. As detailed in the Sect. 3.2, when exceedance probabilities are time dependent, the flood risk (refer to Eq. 5b, Table 1) is a function of both the length of the design life and the implicit period of operation. Figure 5 plots the risk of flood vs. project life for three time periods, 1950 to 1999, 2000 to 2049 and 2050 to 2099. In other words, this is the risk of a flood exceeding 37 600 cfs in the next n years if you are standing in 1950, 2000 or 2050. The median and interquartile ranges show the distribution of the 234 climate projections simulated. Here we use the interquartile range, as opposed to the 5th and 95th percentile, to focus on the central tendencies of each time period and not the variability between projections.

For both Farad and Reno there is a clear positive shift in flood risk between the three time periods. In all cases the median risk for each subsequent time period falls outside the interquartile range of the preceding time period although the prediction spread for Reno is greater than Farad. It is important to note that the flood risk is actually higher at Farad than Reno in both the historical and future periods despite the fact that the observed flow distributions at the two stations are very similar (refer to Fig. 2). This shift between Farad and Reno is caused by the differences in the shape parameters (refer to Table 3). Farad has a heavier tailed distribution and therefore flood risks are increased. The sensitivity of the model parameters (and the associated flood risk) to small differences in the flow and covariate distributions is further demonstrated by Fig. 6.

HESSD
11, 5077–5114, 2014

Figure 6 presents the project life risk from Fig. 5 for three project life periods (10, 20 and 30 years). Boxplots show the non-stationary model results for the 234 climate projections with the different time periods compared side by side. Also, the risk calculated using a stationary GEV model and a stationary LP3 model (i.e., the distribution prescribed by Bulletin 17B; IACWD, 1982) fit to the historical flow data are plotted for reference (blue and red dashed lines respectively). Comparing between these three approaches (non-stationary GEV, stationary GEV and stationary LP3) provides information on the sensitivity of results to model choice and non-stationary parameters. For instance, both stationary models are fit to the same historical flow data so differences between the stationary lines reflect the impact of model choice on estimated risk. Conversely the stationary GEV model (blue line) and the historical non-stationary models (grey boxplot) have the same model form and cover the same time period; the only difference is the addition of covariates to estimate model parameters. Thus differences between these two show the effect of model parameter changes from the non-stationary approach. Finally, variability between the boxplots for a given design period demonstrates the evolution of risk over time (i.e., the impact of climate trends on risk). The latter (i.e., changing risk over time), is the purpose of this analysis, however before assessing trends over time, we must first discuss the impact of model choice and parameters on risk estimates.

For both of the stationary methods, the risk increases with project life following Eq. (5a) from Table 1. The distinction between these lines and the non-stationary approaches is that, with the stationary approach, a single exceedance probability is calculated for the given flood magnitude and this probability is assumed to remain constant throughout the design life. Also, for both stationary approaches the model is fit directly to the historical one day maximum flow distribution and no covariates are required (note that stationary models are not fit to the future time periods because this would require future simulated flows). Comparing between the GEV (blue line) and the LP3 (red line) stationary models there is a 10–20 % increase in risk between the two

HESSD
11, 5077–5114, 2014

models. This difference is purely a function of model form and highlights the sensitivity of the risk calculations to model choice.

Contrasting the difference between the stationary (blue line) and the non-stationary GEV for the historical time period (grey boxplot) illustrates the effect of adding non-stationary parameters to a given model form. Recall that in both cases the GEV model is fit to the historical simulated flows. However, for the stationary approach, model fitting results in a single set of parameters (location, scale and shape) whereas with the non-stationary approach we derive the shape parameter and a set of coefficients for linear models to determine the location and scale parameters based on precipitation and temperature values. Thus, for the non-stationary approach, different location and scale parameters are calculated for every historical cool season month and GCM simulation (234).

Overall, there is close agreement between the stationary (S) and average non-stationary (NS) location parameters (6.55 S vs. 6.64 NS at Farad and 6.63 S vs. 6.78 NS at Reno). However, for both gauges the scale parameter is lower with the non-stationary approach (1.30 S vs. 0.94 NS at Farad and 1.28 S vs. 0.96 NS at Reno). At Reno the shape parameter is similar (−0.24 S vs. −0.27 NS), but at Farad the difference is somewhat larger (−0.24 S vs. −0.18 NS). Differences in model parameters are reflected in the distance between the stationary GEV model (blue line) and the median historical non-stationary GEV boxplots (center of the grey boxplots) in Fig. 6. For Reno the stationary line is closer to the historical boxplots. However, at Farad, the non-stationary boxplots are consistently higher than the stationary line. The larger differences between the stationary and non-stationary models for Farad result from changes in the shape parameter between the stationary and non-stationary model fits. This change demonstrates the sensitivity of model results to changes in model parameters.

As with Fig. 5, Fig. 6 shows significant increases in risk moving into the future and subsequently larger differences between the stationary and non-stationary approach. By the second future period the differences between the stationary and non-stationary

HESSD
11, 5077–5114, 2014

models can be as much as 50 % or more. For both gauges, difference in risk between the non-stationary and stationary approaches grows over time, indicating greater potential to underestimate risk looking further into the future if non-stationary parameters are not adopted.

Although the figures are not shown here, results were also grouped by RCPs to analyze connections between greenhouse gas emission rates and changes in flood risk. We observed no clear trend in flood risk based on the different RCPs. This indicates that the variability between GCM model form and initial conditions likely overwhelms the influence of greenhouse gas emissions when comparing between scenarios. In other words, the variability between projections within any RCP scenario is larger than the difference between RCP scenarios.

Given the sensitivity of projected risk to model parameters, an obvious question is whether increases in risk over time are similarly sensitive. For the 37 600 cfs flood plotted in Fig. 6, the increased risk with added project life (i.e., 20 years vs. 10 years) is greater with the non-stationary models than the stationary one at both stations. This is intuitive, given the increased flood risk with time demonstrated in Fig. 5 for the non-stationary models. Although, Farad has higher risk overall, the relative increase in risk between time periods is similar between the two stations. For example, the median ten year flood risk increases by 21 % for Farad comparing between the first (1950–1999) and second (2000–2049) time periods compared to 29 % for Reno.

Next, analysis is expanded to a range of flood magnitudes. Figure 7 plots the flood risk over a ten year project life starting in 1950, 2000, and 2050 for flood values ranging from 10 000 to 50 000 cfs. As would be expected, the ten year flood risk decreases with increasing flood rate. The shapes of the curves are slightly different between Farad and Reno; flood risk decreases more sharply with increased flow at Reno than Farad. Again this behavior is a function of the shape of the distribution. Despite these differences, both gauges display clear shifts between time periods similar to Fig. 5. Here again, the median risk for each subsequent period consistently falls outside the interquartile range of the preceding period.

HESSD
11, 5077–5114, 2014

Changes in the median flood risk (i.e., differences between the solid lines on Fig. 7) between each future period and the historical period are plotted in Fig. 8 for both gauges. As would be expected based on the qualitative differences in Fig. 7, the shape of the Farad and Reno difference curves are slightly different. However, the salient point for this analysis is that the increased risk between periods is generally within 10 % between the two stations. Overall the increased risk between the first future period (2000–2050) and the historical period (1950–1999) is between 10 and 20 % for flows from 20 000 to 40 000 cfs. Similarly, the increased risk from the historical period to the second future period (2050–2099) is between 30 and 50 %. Differences for the highest and lowest flows are difficult to assess because the values asymptotically approach the upper and lower limits of risk (i.e., 0 and 100 %).

5 Summary and conclusions

The analysis presented is unique in its incorporation of non-stationary GEV analysis using CMIP 5 GCM simulations and the design life level risk assessment. We present our findings as a relevant case study and an example application of recent developments in non-stationary flood assessment. Lacking sufficient unregulated flow data, we simulate historical floods using the VIC model. Subsequently, we use the simulated floods to fit non-stationary GEV models with downscaled monthly precipitation and temperature as covariates. Although there are some discrepancies between individual simulated and observed floods, we demonstrate that the VIC model adequately captures the range of flood magnitudes. Furthermore, we show that that the GEV modeled historical floods are in good agreement with both the VIC simulated floods and the published flood events (USACE, 2013).

Discrepancies between historical and simulated events often result from the monthly time step used for covariates. This can affect the ability to model floods that are generated by precipitation that occurs in two months. Also, because the climate variables are monthly aggregates, and not event based, large floods can be generated in months with

HESSD
11, 5077–5114, 2014

high precipitation even if that precipitation does not occur in one concentrated event. Despite these differences, comparison with historical floods demonstrate that the GEV model sufficiently encompasses historical flood magnitudes, even if some individual historical events are not matched exactly.

Using the derived non-stationary GEV models, we generate flood distributions for 234 CMIP5 GCM climate simulations from 1950 to 2099. For the historical one-day design flood magnitude of 37 600 cfs, results show significant increases in the frequency of high flow events in the future. From a water management standpoint this finding translates directly to increased flood risk. For example, we calculate a 21 % (29 %) increase risk of a 37 600 cfs flood over a 10 year design life for Farad (Reno) from the historical time period to the first future period, and similar increases from the first future period to the second. Increased risk between time periods is also relatively consistent for longer design life periods and similar shifts in flood risk are noted across a range of flood magnitudes. For both stations the increased risk from the historical to the first future period is between 10 and 20 % and from the historical to the second future period is between 30 and 50 % for floods ranging from 20 000–40 000 cfs.

The significant increases in flood risk through time indicate the importance of non-stationary flood frequency analysis for future infrastructure planning and the potential to underestimate risk when stationarity is assumed. For both stations the difference between the stationary and no-stationary approach increases over time. By the second future period differences in risk calculations between the stationary and non-stationary models can be 50 % or larger. This finding is in keeping with a number of recent studies (e.g., Griffis and Stedinger, 2007; Katz et al., 2002; Towler et al., 2010) that have highlighted potential applications for non-stationary analysis of flood frequency.

An important consideration for this approach is the sensitivity of results to model parameters. In all cases the flood risk is higher at Farad than Reno due to the heavier tailed distribution that was fit. Estimated model parameters differed by station despite the fact that the flow, precipitation and temperature distributions for both locations are very similar. While these changes affected the overall risk projections, the relative

HESSD
11, 5077–5114, 2014

increase in risk over time remained consistent between stations. This indicates that the more robust metric from this analysis is the relative increase in flood risk and not the absolute values. This finding is further supported by the fact that absolute flood risk estimates could be impacted by model bias. By focusing on differences in risk we specifically highlight the impact of non-stationarity on risk assessment, as opposed to parameter sensitivity. Similarly, it is important to note that this analysis is based on unregulated flow estimates and does not include infrastructure development or operation. As such results indicate the potential increase in the underlying natural flood risk and not the potential increase in flood damages.

References

Akaike, H.: New look at statistical-model identification, IEEE T. Automat. Contr., 19, 716–723, 1974.

Allan, R. P.: Climate change: human influence on rainfall, Nature, 470, 344–345, 2011.

Cayan, D. R., Redmond, K. T., and Riddle, L. G.: ENSO and hydrologic extremes in the western United States, J. Climate, 12, 2881–2893, 1999.

Cayan, D. R., Kammerdiener, S. A., Dettinger, M. D., Caprio, J. M., and Peterson, D. H.: Changes in the onset of spring in the western United States, B. Am. Meteorol. Soc., 82, 399–415, 2001.

Christensen, N. S. and Lettenmaier, D. P.: A multimodel ensemble approach to assessment of climate change impacts on the hydrology and water resources of the Colorado River Basin, Hydrol. Earth Syst. Sci., 11, 1417–1434, doi:10.5194/hess-11-1417-2007, 2007.

Christensen, N. S., Wood, A. W., Lettenmaier, D. P., and Palmer, R. N.: Effects of climate change on the hydrology and water resources of the Colorado river basin, Climatic Change, 62, 337–363, 2004.

Das, T., Pierce, D. W., Cayan, D. R., Vano, J. A., and Lettenmaier, D. P.: The importance of warm season warming to western U.S. streamflow changes, Geophys. Res. Lett., 38, L23403, doi:10.1029/2011GL049660, 2011.

Dettinger, M. D. and Cayan, D. R.: Large-scale atmospheric forcing of recent trends toward early snowmelt runoff in California, J. Climate, 8, 606–623, 1995.

HESSD
11, 5077–5114, 2014

Douglas, E. M., Vogel, R. M., and Kroll, C. N.: Trends in floods and low flows in the United States: impact of spatial correlation, J. Hydrol., 240, 90–105, 2000.
Easterling, D. R., Meehl, G. A., Parmesan, C., Changnon, S. A., Karl, T. R., and Mearns, L. O.: Climate extremes: observations, modeling and impacts, Science, 289, 2068–2074, 2000.
Franks, S. W.: Identification of a change in climate state using regional flood data, Hydrol. Earth Syst. Sci., 6, 11–16, doi:10.5194/hess-6-11-2002, 2002.
Gangopadhyay, S., Pruitt, T., Brekke, L. D., and Raff, D. A.: Hydrologic projections for the western United States, EOS, 92, 441–452, 2011.
Gilleland, E. and Katz, R. W.: New software to analyze how extremes change over time, EOS, 92, 13–14, 2011.
Gilroy, K. L. and McCuen, R. H.: A nonstationary flood frequency analysis method to adjust for future climate change and urbanization, J. Hydrol., 414–415, 40–48, 2012.
Griffis, V. and Stedinger, J. R.: Incorporating climate change and variability into Bulletin 17B LP3 model, paper presented at ASCE World Env. and Water Resour. Congress, Tampa, Florida, USA, 2007.
Gutowski, W. J., Hegerl, G. C., Holland, G. J., Knutson, T. R., Mearns, L. O., Stouffer, R. J., Webster, P. J., Wehner, M. F., and Zwiers, F. W.: Causes of Observed Changes in Extremes and Projections of Future Changes in Weather and Climate Extremes in a Changing Climate, Regions of Focus: North America, Hawaii, Caribbean, and US Pacific IslandsRep., Washington, D.C., 2008.
IACWD – Interagency Advisory Committee on Water Data: Guidelines for determining flood flow frequency: Bulletin 17B of the Hydrology Subcommittee, Office of Water Data Coordination, US Geological Survey, Reston, VA, 183 pp., 1982.
Jain, S. and Lall, U.: Floods in a changing climate: does the past represent the future?, Water Resour. Res., 37, 3193–3205, 2001.
Katz, R. W.: Statistics of extremes in climate change, Climatic Change, 100, 71–76, 2010.
Katz, R. W., Parlange, M. B., and Naveau, P.: Statistics of extremes in hydrology, Adv. Water Resour., 25, 1287–1304, 2002.
Kunkel, K. E.: North American trends in extreme precipitation, Nat. Hazards, 29, 291–305, 2003.
Liang, X., Lettenmaier, D. P., Wood, E. F., and Burges, S. J.: A simple hydrologically based model of land surface water and energy fluxes for general circulation models, J. Geophys. Res., 99, 14415–14428, 1994.

HESSD
11, 5077–5114, 2014

Liang, X., Wood, E. F., and Lettenmaier, D. P.: Surface soil moisture parameterization of the VIC-2L model: evaluation and modification, Global Planet. Change, 13, 195–206, 1996.
Madsen, T. and Figdor, E.: When it Rains it Pours – Global Warming and the Rising Frequency of Extreme Precipitaiton in the U.S., Environmental America Research and Policy Center, Boston, MA, 2007.
Maidment, D. R.: Handbook of Hydrology, McGraw-Hill, New York, 1993.
Maurer, E. P., Wood, A. W., Adam, J. C., Lettenmaier, D. P., and Nijssen, B.: A long-term hydrologically-based dataset of land surface fluxes and states for the conterminous United States, J. Climate, 15, 3237–3252, 2002.
Maurer, E. P., Brekke, L. D., Pruitt, T., and Duffy, P. B.: Fine-resolution climate projections enhance regional climate change impact studies, EOS T. Am. Geophys. Un., 88, 504, doi:10.1029/2007EO470006, 2007.
Meehl, G. A., Karl, T., Easterling, D. R., Changnon, S., Pielke Jr., R., Changnon, D., Evans, J., Groisman, P. Y., Knutson, T. R., Kunkel, K. E., Mearns, L. O., Parmesan, C., Pulwarty, R., Root, T., Sylves, R. T., Whetton, P., and Zwiers, F.: An introduction to trends in extreme weather and climate events: observations, socioeconomic impact, terrestrial ecological impacts, and model projections, B. Am. Meteorol. Soc., 81, 413–416, 2000.
Milly, P. C. D., Betancourt, J., Falkenmark, M., Hirsch, R. M., Kundzewicz, Z. W., Lettenmaier, D. P., and Stouffer, R. J.: Stationarity is dead: whither water management, Science, 319, 573–574, 2008.
Min, S.-K., Zhang, X., Zwiers, F. W., and Hegerl, G. C.: Human contribution to more-intense precipitation extremes, Nature, 470, 378–381, 2011.
Mote, P. W., Hamlet, A. F., Clark, M. P., and Lettenmaier, D. P.: Declining mountain snowpack in western North America, B. Am. Meteorol. Soc., 39–49, doi:10.1175/BAMS-86-1-39, 2005.
Mullet, C. J., O'Gorman, P. A., and Back, L. E.: Intensification of precipitation extremes with warming in a cloud resolving model, J. Climate, 24, 2784–2800, 2011.
Nijssen, B., Lettenmaier, D. P., Liang, X., Wetzel, S. W., and Wood, E. F.: Streamflow simulation for continental-scale river basins, Water Resour. Res., 33, 711–724, 1997.
O'Gorman, P. A. and Schneider, T.: The physical basis for increases in precipitaiton extremes in simulations of 21st century climate change, P. Natl. Acad. Sci. USA, 106, 14773–14777, 2009.

HESSD
11, 5077–5114, 2014

Pall, P., Aina, T., Stone, D. A., Stott, P. A., Nozawa, T., Hilberts, A. G. J., Lohmann, D., and Allen, M. R.: Anthropogenic greenhouse gas contribution to flood risk in England and Wales in autumn 2000, Nature, 470, 382–385, 2011.

Payne, J. T., Wood, A. W., Hamlet, A. F., Palmer, R. N., and Lettenmaier, D. P.: Mitigating the effects of climate change on the water resources of the Columbia River basin, Climatic Change, 62, 233–256, 2004.

Pierce, D. W., Das, T., Cayan, D. R., Maurer, E. P., Miller, N. L., Bao, Y., Kanamitsu, M., Yoshimura, K., Snyder, M. A., Sloan, L. C., Franco, G., and Tyree, M.: Probabilistic estimates of future changes in California temperature and precipitation using statistical and dynamical downscaling, Clim. Dynam., 40, 839–856, 2012.

Raff, D. A., Pruitt, T., and Brekke, L. D.: A framework for assessing flood frequency based on climate projection information, Hydrol. Earth Syst. Sci., 13, 2119–2136, doi:10.5194/hess-13-2119-2009, 2009.

Ralph, F. M. and Dettinger, M. D.: Historical and National perspectives on extreme west coast precipitation associated with atmospheric rivers during December 2010, B. Am. Meteorol. Soc., 93, 783–790, 2012.

Reclamation: Downscaled CMIP3 and CMIP5 Climate Projections: Release of Downscaled CMIP5 Climate Projections, Comparison with Preceding Information, and Summary of User Needs, Downscaled CMIP3 and CMIP5 Climate and Hydrology Projections, US Department of the Interior, Bureau of Reclamation, Technical Service Center, Denver, Colorado, 116 pp., 2013.

Regonda, S. K., Rajagopalan, B., Clark, M., and Pitlick, J.: Seasonal cycle shifts in hydroclimatology over the western U.S., J. Climate, 18, 372–384, 2005.

Rootzén, H. and Katz, R. W.: Design life level: quantifying risk in a changing climate, Water Resour. Res., 49, 5964–5972, 2013.

Salas, J. and Obeysekera, J.: Revisiting the concepts of return period and risk for nonstationary hydrologic extreme events, J. Hyrol. Eng., 19, 554–568, 2014.

Small, D., Islam, S., and Vogel, R. M.: Trends in precipitation and streamflow in the eastern U.S.: paradox or perception?, Geophys. Res. Lett., 33, L03403, doi:10.1029/2005GL024995, 2006.

Stokes, J.: Draft Farad Diversion Dam Replacement Project Environmental Impact ReportRep., State Water Resources Control Board, Sacramento, CA, 2002.

HESSD
11, 5077–5114, 2014

Sun, Y., Solomon, S., Dai, A., and Portmann, R. W.: How often will it rain?, J. Climate, 20, 4801–4818, 2007.
Taylor, K. E., Stouffer, R. J. and Meehl, G. A.: A summary of the CMIP5 experiment design, B. Am. Meteorol. Soc., 93, 485–498, 2012.
Towler, E., Rajagopalan, B., Gilleland, E., Summers, R. S., Yates, D., and Katz, R. W.: Modeling hydrologic and water quality extremes in a changing climate: a statistical approach based on extreme value theory, Water Resour. Res., 46, W11504, doi:10.1029/2009WR008876, 2010.
USACE: Truckee Meadows Flood Control Project, Nevada: Draft General Reevaluation ReportRep., US Army Corps of Engineers, Sacramento, 2013.
Van Rheenen, N. T., Wood, A. W., Palmer, R. N., and Lettenmaier, D. P.: Potential implications of PCM climate change scenarios for Sacramento-San Joaquin River Bain hydrology and water resources, Climatic Change, 62, 257–281, 2004.
Villarini, G., Serinaldi, F., Smith, J. A., and Krajewski, W. F.: On the stationarity of annual flood peaks in the continental United States during the 20th century, Water Resour. Res., 45, W08417, doi:10.1029/2008WR007645, 2009.
Vogel, R. M., Yaindl, C., and Walter, M.: Nonstationarity: flood magnification and recurrence reduction factors in the United States, JAWRA, 47, 464–474, 2011.
Walter, M. and Vogel, R. M.: Increasing trends in peak flows in the northeastern United States and their impacts on design, paper presented at 2nd Joint Federal Interagency Conference, Las Vegas, NV, 2010.
Wood, A. W., Leung, L. R., Sridhar, V., and Lettenmaier, D. P.: Hydrologic implications of dynamical and statistical approaches to downscaling climate model outputs, Climatic Change, 62, 189–216, 2004.
Wu, H., Adler, R. F., Tian, Y., Juffman, G. J., Li, H., and Wang, J. J.: Real-time global flood estimation using satellite-based precipitation and a coupled land surface routing model, Water Resour. Res., 50, 2693–2717, doi:10.1002/2013WR014710, 2014.

HESSD
11, 5077–5114, 2014

Table 1. Flood calculations using stationary and non-stationary distributions (adapted from Salas and Obeysekera, 2014).

Eqn. #	Description	a. Stationary	b. Non Stationary
1	Exceedance probability (Probability of flood[a] occurring in year x)	p	p_x
2	Probability of the first flood occurring in year x [b]	$f(x) = (1-p)^{x-1}p$	$f(x) = p_x \prod_{t=1}^{x-1} 1 - p_t$
3	Probability of a flood occurring before year x [c]	$F(x) = \sum_{i=1}^{x} f(i)$	
		$F(x) = 1-(1-p)^x$	$F(x) = 1 - \prod_{t=1}^{x} (1-p_t)$
4	Return Period (Expected waiting time between flood occurrences [d,e])	$E(X) = \sum_{x=1}^{\infty} x \cdot P(X = x)$	
		$E(X) = 1/p$	$E(X) = 1 + \sum_{x=1}^{x_{\max}} \prod_{t=1}^{x} (1-P_t)$
5	Probability of a flood occurring before the design life n	$R = P(X \le n) = F(n)$	
		$R = 1-(1-p)^n$	$R = 1 - \prod_{t=1}^{n} (1-p_t)$

[a] Flood is defined as a flow exceeding a predefined threshold.
[b] $f(x)$ = probability density function of X.
[c] $F(x)$ = cumulative distribution function of X.
[d] X = random variable denoting the waiting time for the first flood occurrence.
[e] $x_{\max}$ = time when p_x equals 1.

HESSD
11, 5077–5114, 2014

Table 2. Negative log likelihood (NLLH) scores and p values for pairwise comparisons of different model configurations (P = precipitation only, T = temperature only P and T = both). The selected model for each station is bold.

			Non stationary location			Non stationary scale			Non stationary location and scale		
		Stationary	P and T	P	T	P and T	P	T	P and T	P	T
Station	Metric	1	2	3	4	5	6	7	8	9	10
Farad	NLLH	508.9	422.9	467.1	499.7	487.3	500.9	506.5	**416.4**	462.2	496.9
	p value		< 0.05	< 0.05	< 0.05	< 0.05	< 0.05	< 0.05	< 0.05	< 0.05	< 0.05
Reno	NLLH	505.4	418.4	462.5	496.0	484.4	497.6	503.1	**408.8**	457.4	493.2
	p value		< 0.05	< 0.05	< 0.05	< 0.05	< 0.05	< 0.05	< 0.05	< 0.05	< 0.05
Model # compared to for pval			1	1	1	1	1	1	2	3	4

HESSD
11, 5077–5114, 2014

Table 3. Summary of derived model coefficients (β) from Eqs. (2) and (3) and shape parameters.

	Farad	Reno
$\beta_{0\mu}$	2.155	2.582
$\beta_{1\mu}$	0.175	0.18
$\beta_{2\mu}$	0.115	0.105
$\beta_{0\sigma}$	0.211	0.530
$\beta_{1\sigma}$	−0.013	−0.018
$\beta_{2\sigma}$	0.027	0.017
Shape (ξ)	−0.178	−0.275

HESSD
11, 5077–5114, 2014

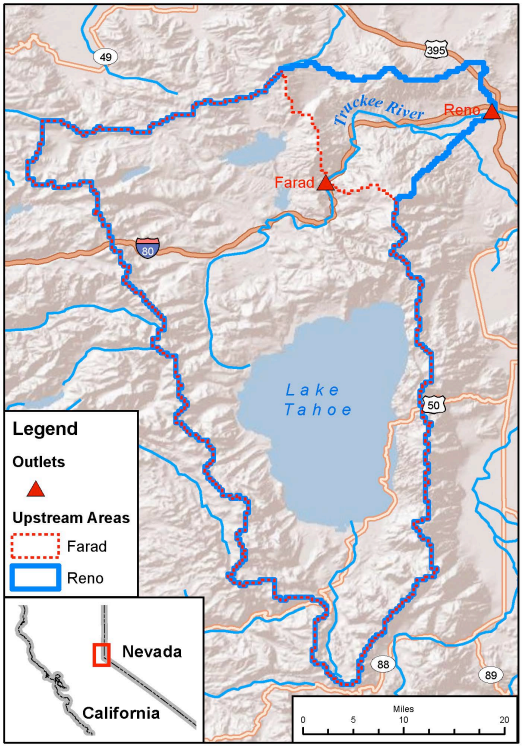

Fig. 1. Map of model domain including the Farad and Reno gauges and their drainage areas.

HESSD
11, 5077–5114, 2014

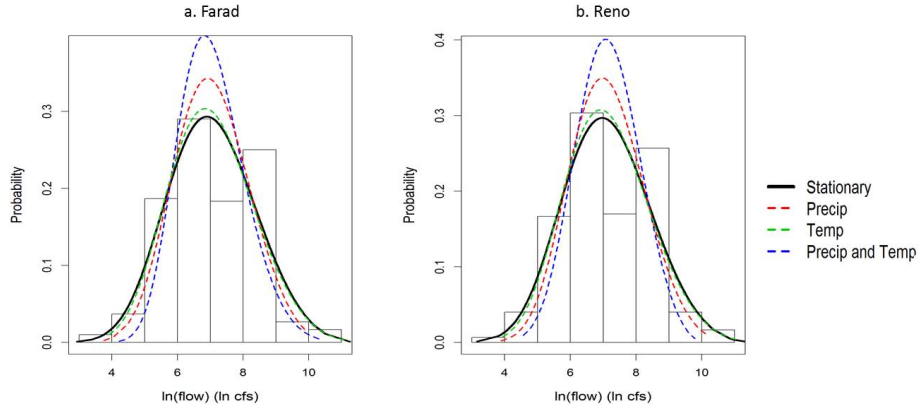

Fig. 2. PDFs of fitted stationary (solid black) and non-stationary (dashed) GEV models compared to historical VIC simulated flow histogram.

HESSD
11, 5077–5114, 2014

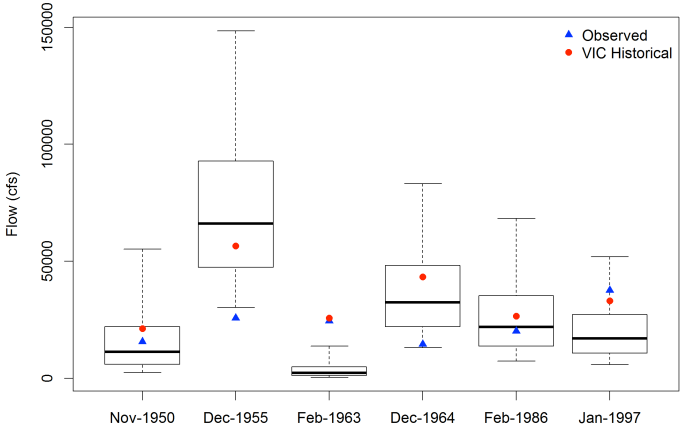

Fig. 3. "Observed" ungauged flow estimated from gauge records (blue triangle) compared with VIC simulated flow (red circles) and the simulated GEV distribution. Boxes span the 25th to 75th percentile of the GEV distribution for a given month and the whiskers extend to the 5th and 95th percentiles.

HESSD
11, 5077–5114, 2014

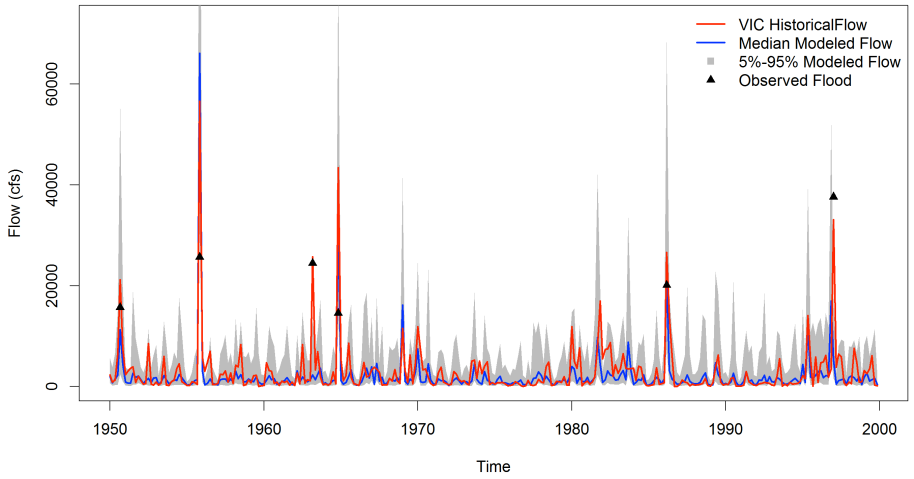

Fig. 4. VIC simulated one-day flood maximums for November through April 1950 to 1999 (red lines) compared with the historical GEV distributions (blue line is median and grey shading is the 5th to 95th percentile range) and the six observed flow rates.

HESSD
11, 5077–5114, 2014

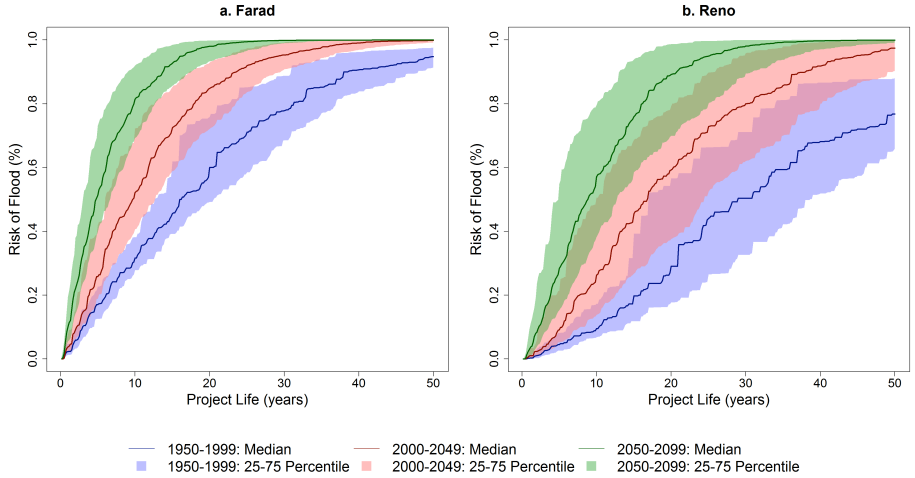

Fig. 5. Risk of one day flood exceeding historical maximum of 37 600 cfs at Farad and Reno. Solid lines represent the median risk of the 234 climate projections and shading covers the interquartile range (i.e., 25th to 75th percentile).

HESSD
11, 5077–5114, 2014

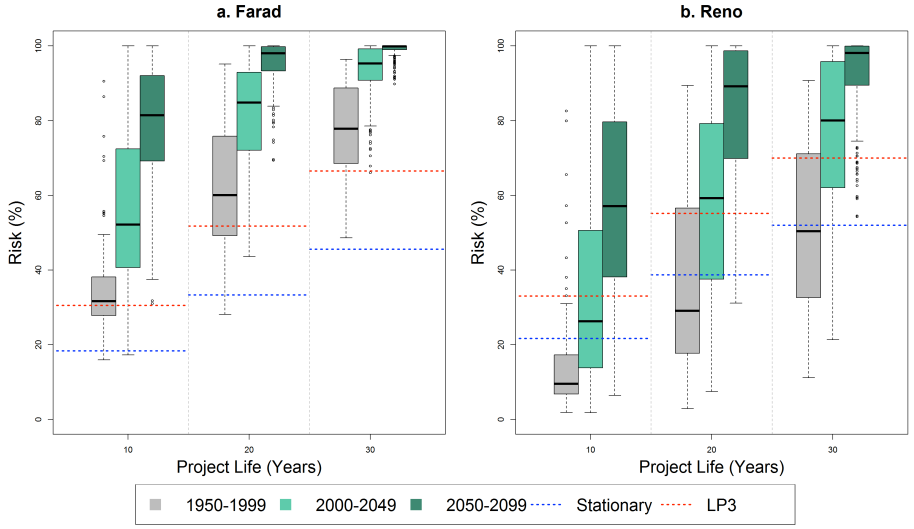

Fig. 6. Boxplots of the risk of a one-day flood exceeding 37 600 cfs for three project life lengths (10, 20 and 30 years). Results are grouped by time period (1950–1999, 2000–2049 and 2050–2099). Blue dashed lines show the flood risk calculated from the stationary GEV model fit to the historical data.

HESSD
11, 5077–5114, 2014

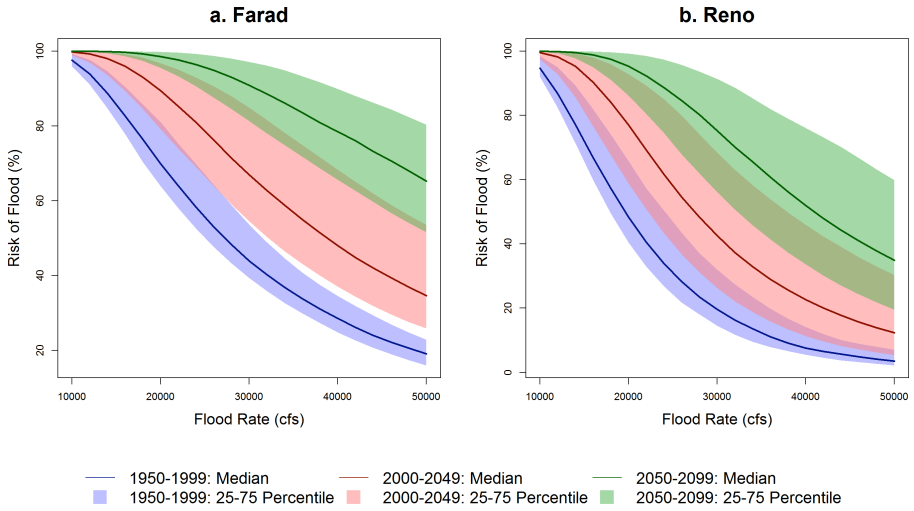

Fig. 7. Risk of flood in a ten year project life vs. median one day flood rate **(a)** Farad and **(b)** Reno for three time periods 1950–1999 (blue), 2000–2049 (red) and 2050–2099 (green). Solid lines represent the median of the 234 climate projections and shading covers the interquartile range (i.e., 25th to 75th percentile).

HESSD
11, 5077–5114, 2014

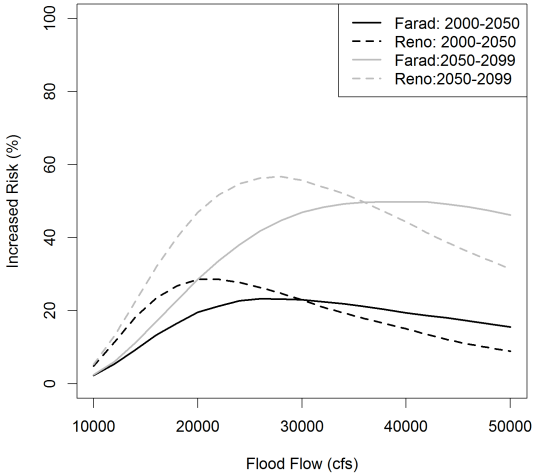

Fig. 8. Increased flood risk for a 10 year project life from the historical period (1950–1999) to each of the two future periods 2000–2050 (black) and 2050–2099 (grey). Farad is plotted with a solid line and Reno is a dashed line.

HESSD
11, 5077–5114, 2014